Acetylcholine-synthesizing macrophages in subcutaneous fat are regulated by β2-adrenergic signaling

Alexander J Knights[1,*,†] , Shanshan Liu[1,†], Yingxu Ma[1,2], Victoria S Nudell[3], Eric Perkey[1,4], Matthew J Sorensen[5], Robert T Kennedy[5,6], Ivan Maillard[7] , Li Ye[3], Heejin Jun[1,**,†] & Jun Wu[1,8,***]

Abstract

Non-neuronal cholinergic signaling, mediated by acetylcholine, plays important roles in physiological processes including inflammation and immunity. Our group first discovered evidence of non-neuronal cholinergic circuitry in adipose tissue, whereby immune cells secrete acetylcholine to activate beige adipocytes during adaptive thermogenesis. Here, we reveal that macrophages are the cellular protagonists responsible for secreting acetylcholine to regulate thermogenic activation in subcutaneous fat, and we term these cells cholinergic adipose macrophages (ChAMs). An adaptive increase in ChAM abundance is evident following acute cold exposure, and macrophage-specific deletion of choline acetyltransferase (ChAT), the enzyme for acetylcholine biosynthesis, impairs the cold-induced thermogenic capacity of mice. Further, using pharmacological and genetic approaches, we show that ChAMs are regulated via adrenergic signaling, specifically through the β2 adrenergic receptor. These findings demonstrate that macrophages are an essential adipose tissue source of acetylcholine for the regulation of adaptive thermogenesis, and may be useful for therapeutic targeting in metabolic diseases.

Introduction

Adipose tissue is a dynamic endocrine organ known to actively function in response to environmental and endogenous cues to regulate systemic metabolism and energy expenditure (Scheja & Heeren, 2019). The various discrete and subtle adipose tissue depots that develop in rodents and humans alike are home to a diversity of cell types, all of which participate in elaborate crosstalk to sustain homeostatic functions. Parenchymal adipocytes reside amidst a rich stromal vascular compartment comprised of immune cells, fibroblasts, mesenchymal stem cells, progenitors, endothelial cells, and various other cell types. We are gradually uncovering the interconnected roles of these resident cell populations, and immune cells in particular have been the subject of intensive research efforts aimed at understanding their contribution to tissue and organismal homeostasis.

The capacity for adipose tissue to undertake adaptive thermogenesis, whereby adipocytes expend energy instead of storing it, is now well recognized. In the past decade, we have uncovered important roles for immune cells in regulating activation of thermogenic adipose tissue (brown and beige fat) (Villarroya et al, 2018). γδ T cells have recently been shown to modulate adipose innervation to facilitate adaptive thermogenesis (Kohlgruber et al, 2018; Hu et al, 2020), and group 2 innate lymphoid cells secrete methionine enkephalin peptides that drive beiging (Brestoff et al, 2015). On the contrary, adipose-resident lymphocytes can inhibit thermogenic activation via production of interleukin-10 (Rajbhandari et al, 2018; Rajbhandari et al, 2019) and mast cell-derived serotonin also functions to impair the thermogenic response (Zhang et al, 2019; Yabut et al, 2020).

Adipose-resident macrophages were originally thought to produce catecholamines, namely norepinephrine (NE), to potentiate

1 Life Sciences Institute, University of Michigan, Ann Arbor, MI, USA
2 Department of Cardiology, The Second Xiangya Hospital, Central South University, Changsha, Hunan, China
3 Department of Neuroscience, The Scripps Research Institute, La Jolla, CA, USA
4 Graduate Program in Cellular and Molecular Biology, University of Michigan, Ann Arbor, MI, USA
5 Department of Chemistry, University of Michigan, Ann Arbor, MI, USA
6 Department of Pharmacology, University of Michigan, Ann Arbor, MI, USA
7 Division of Hematology-Oncology, Department of Medicine, University of Pennsylvania Perelman School of Medicine, Philadelphia, PA, USA
8 Department of Molecular and Integrative Physiology, University of Michigan Medical School, Ann Arbor, MI, USA
  *Corresponding author. Tel: +1 734 763 6790; Email: aknights@umich.edu
  **Corresponding author. Tel: +1 734 763 6790; Email: junhee@umich.edu
  ***Corresponding author. Tel: +1 734 763 6790; Email: wujunz@umich.edu
  †These authors contributed equally to this work.

adaptive thermogenesis (Nguyen *et al*, 2011). This put forward macrophages as an additional source of catecholamines in fat alongside sympathetic innervation, whose production of catecholamines is a well-established mediator between environmental cues such as cold stimulus and the thermogenic response in adipose tissue (Morrison, 2016). However, these findings were later brought into question by several groups who showed that adipose-resident macrophages lack tyrosine hydroxylase, the enzyme required to synthesize NE; instead, a subset of sympathetic neuron-associated macrophages was revealed to contribute to catecholamine degradation in adipose tissue (Camell *et al*, 2017; Fischer *et al*, 2017; Pirzgalska *et al*, 2017).

While thermogenic activation is heavily dependent upon sympathetic innervation of fat, which mediates adrenergic signaling via catecholamine production, there is no evidence of parasympathetic innervation in adipose tissue, which relies on acetylcholine as its primary mediator (Giordano *et al*, 2006). Non-neuronal cholinergic signaling networks have emerged in several tissues as mediators of homeostasis, and their dysregulation has been implicated in various pathologies (Beckmann & Lips, 2013). Cholinergic immune cells perform anti-inflammatory functions in the spleen, co-ordinate local innate immune cell recruitment, and assist in the antiviral T-cell response (Rosas-Ballina *et al*, 2011; Reardon *et al*, 2013; Cox *et al*, 2019). Our group recently discovered the first evidence of a non-neuronal cholinergic pathway in adipose tissue, in which resident immune cells secrete acetylcholine that sustains activation of beige adipocytes expressing the nicotinic acetylcholine receptor, alpha 2 subunit (CHRNA2) (Jun *et al*, 2018).

Here, we describe a previously unidentified discrete population of cholinergic adipose macrophages (ChAMs) that secrete acetylcholine to drive adaptive thermogenesis. Using flow cytometry and three-dimensional imaging, we profiled the cellular and spatial landscape of non-neuronal cholinergic circuitry in subcutaneous adipose tissue. Following cold exposure, inguinal ChAMs increased in abundance, and ablation of choline acetyltransferase (ChAT, the enzyme for acetylcholine biosynthesis) selectively in macrophages abolished induction of acetylcholine secretion after cold. Further, we demonstrated that macrophage-specific ChAT deletion impaired the thermogenic capacity of subcutaneous fat in response to cold stress. Finally, we showed that the activity of ChAMs is regulated via the β_2 adrenergic receptor (AR) using pharmacological and genetic approaches both *in vitro* and *in vivo*. The identification of this novel cholinergic macrophage population in subcutaneous adipose tissue represents an important contribution to our understanding of the cellular repertoire that regulates adaptive thermogenesis. Harnessing these cells and the molecular mechanisms that mediate their function to activate energy expenditure may provide new avenues for therapeutic intervention in metabolic disorders such as obesity and type 2 diabetes.

Results

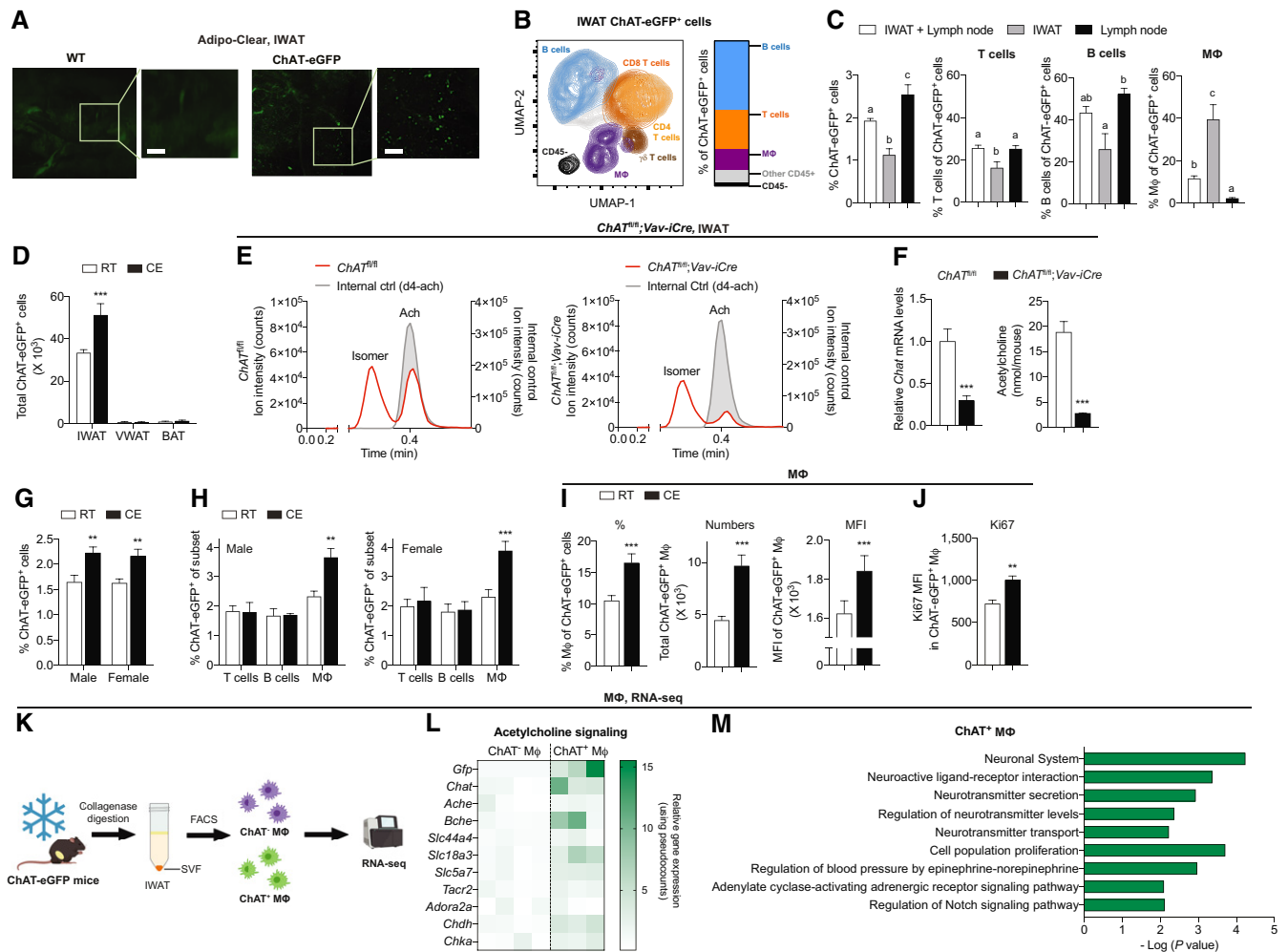### Acetylcholine-synthesizing macrophages reside in subcutaneous fat

Subcutaneous fat lacks parasympathetic innervation (Giordano *et al*, 2006), resulting in the absence of local neuronally derived acetylcholine. Instead, we have shown that hematopoietic cells residing within the stromal vascular fraction (SVF) of subcutaneous fat express ChAT and thus serve as a local source of acetylcholine (Jun *et al*, 2018).

To investigate the spatial landscape of this non-neuronal cholinergic niche in subcutaneous fat, we performed three-dimensional whole adipose tissue imaging in ChAT-eGFP reporter mice. Using the Adipo-Clear method (Chi *et al*, 2018), we revealed that ChAT-eGFP$^+$ acetylcholine-synthesizing cells are interspersed throughout the subcutaneous inguinal fat pad (IWAT) (Figs 1A and EV1A and Movie EV1). Dimensionality reduction of high-parameter flow cytometric analysis confirmed the composition of the ChAT-eGFP$^+$ population as being primarily cells of hematopoietic origin, including T cells, B cells and macrophages (Figs 1B and EV1). The distribution of these ChAT-eGFP$^+$ cell subsets was analyzed using surface marker-based clustering, and their proportional breakdown is in line with our previous observations (Table EV1), including a notable absence of any ChAT-eGFP$^+$ eosinophils or neutrophils (Fig EV1E) (Jun *et al*, 2018). Further analysis revealed that ChAT-eGFP$^+$ cells were distributed throughout the depot, in both fat tissue and within the lymph node. Interestingly, ChAT-eGFP$^+$ macrophages are predominantly localized in adipose tissue compared with lymph node (Fig 1C). Flow cytometric analysis of ChAT-eGFP$^+$ hematopoietic cells across adipose depots showed a highly enriched population residing in IWAT compared with visceral fat (VWAT) and brown fat (BAT) (Fig 1D). Further, acute cold exposure increased the abundance of ChAT-eGFP$^+$ hematopoietic cells in IWAT, suggesting that these cells play a role in the response to cold temperature. Generation of a ChAT-eGFP *ChAT-Cre;tdTomato* double reporter mouse revealed overlap between constitutively active ChAT-eGFP$^+$ hematopoietic cells and indelibly labeled tdTomato$^+$ cells in IWAT (Fig EV1C).

Hematopoietic-specific deletion of *ChAT* in *ChAT$^{fl/fl}$;Vav-iCre* mice resulted in significantly reduced levels of *Chat* transcript in IWAT and in the ablation of acetylcholine secretion by IWAT SVF cells, as measured using liquid chromatography coupled to tandem mass spectrometry (LC-MS/MS) (Figs 1E and F, and EV2A–D). Both male and female ChAT-eGFP$^+$ mice exhibited a significant increase in the percentage of ChAT-eGFP$^+$ cells in IWAT following acute cold exposure (Fig 1G). Further, after cold exposure no changes were observed in the proportion of IWAT T cells or B cells that were ChAT-eGFP$^+$; however, ChAT$^+$ macrophages doubled as a percentage of total macrophages following cold in male and female mice, and correspondingly also increased in total number and proportion of all ChAT-eGFP$^+$ cells (Figs 1H and I, and EV2E). No significant changes in the total number or proportion of ChAT-eGFP$^+$ T cells, B cells, or other immune cells were evident (Fig EV2F–H). ChAT-eGFP expression, as measured by median fluorescence intensity (MFI), was higher in macrophages following cold exposure (Fig 1I), and expression of the proliferation marker Ki67 was also elevated in ChAT-eGFP$^+$ macrophages after cold compared with room temperature (Figs 1J and EV2I).

Sorted ChAT-eGFP$^+$ hematopoietic cells highly expressed *Chat* and other vital machinery to undertake cholinergic signaling compared with ChAT-eGFP$^-$ cells (Fig EV2K). Of the major cholinergic cell types in IWAT, macrophages exhibited the highest basal *Chat* expression compared with T cells and B cells (Fig EV2L). Functional cholinergic signaling was further evidenced by transcriptomic

Figure 1. Acetylcholine-synthesizing macrophages reside in subcutaneous fat.

A   Three-dimensional imaging of WT and ChAT-eGFP IWAT using the Adipo-Clear method (Chi *et al*, 2018) and light-sheet fluorescence microscopy. Whole IWAT was stained with Alexa Fluor 488-conjugated anti-GFP antibody to visualize ChAT-eGFP-expressing cells. High-magnification sections are shown to the right of each sample. Scale bars: 100 µm.

B   UMAP plot displaying the profile of ChAT-eGFP+ cells from IWAT, analyzed by flow cytometry and combined from four biological replicates. ChAT-eGFP+ cell types are color-coded with accompanying labels, and the percentage breakdown of ChAT-eGFP+ cells is featured in a bar chart to the right. Related to Table EV1. MΦ, macrophages.

C   Left: Percentage of total live cells expressing ChAT-eGFP derived from IWAT (including inguinal lymph node; *n* = 7), IWAT alone (*n* = 8), and lymph node alone (*n* = 8). Right: Proportion of ChAT-eGFP+ cells comprised by T cells, B cells, and MΦ in each tissue type.

D   Total abundance of ChAT-eGFP+ CD45+ hematopoietic cells in IWAT, VWAT, and BAT SVF isolated from ChAT-eGFP mice housed at room temperature (RT) or exposed to 4°C (CE) for 4 h (*n* = 4).

E   LC/MS-MS traces showing acetylcholine (Ach) levels in SVF isolated from *ChAT*fl/fl and *ChAT*fl/fl;*Vau-iCre* IWAT compared with an internal control (d4-Ach).

F   Left: relative mRNA expression of *Chat* in *ChAT*fl/fl and *ChAT*fl/fl;*Vau-iCre* IWAT (*n* = 9). *Chat* expression was analyzed by qPCR and normalized to levels of *Tbp* using the $2^{-\Delta\Delta Ct}$ method. Right: quantification by LC/MS-MS of Ach concentration in SVF isolated from *ChAT*fl/fl and *ChAT*fl/fl;*Vau-iCre* IWAT (*n* = 6).

G   Percentage of total IWAT SVF cells expressing ChAT-eGFP in male (*n* = 6) and female (*n* = 9) ChAT-eGFP mice housed at RT or CE (4 h).

H   Percentage of total IWAT T cells, B cells, and MΦ that express ChAT-eGFP, from male (*n* = 6) and female (*n* = 5 for T cells and B cells; *n* = 8 for MΦ) mice housed at RT or CE (4 h).

I   Left: MΦ as a percentage of all ChAT-eGFP+ cells in IWAT at RT and 4 h CE (*n* = 15). Middle: Total number of ChAT-eGFP+ MΦ at RT and 4 h CE (*n* = 15). Right: ChAT-eGFP median fluorescence intensity (MFI) for ChAT-eGFP+ MΦ at RT and 4 h CE (*n* = 15).

J   MFI for Ki67 in ChAT-eGFP+ MΦ from IWAT at RT and 4 h CE (*n* = 6).

K   Schematic depicting the experimental strategy for transcriptomic profiling of ChAT-eGFP+ and ChAT-eGFP− MΦ from IWAT of mice housed at 4°C for 4 h.

L   Relative expression (pseudocounts) heatmap of genes relevant to acetylcholine signaling in ChAT-eGFP− (*n* = 4) and ChAT-eGFP+ (*n* = 3) MΦ.

M   Biological pathway analysis of significantly enriched genes in ChAT-eGFP+ MΦ.

Data information: In (C), data are presented as mean ± SEM and the letters "a", "b", and "c" indicate *P* < 0.05 between groups (one-way ANOVA). In (D and F–J), data are presented as mean ± SEM where *P < 0.05, **P < 0.01, and ***P < 0.001 (two-tailed Student's *t*-test).

Source data are available online for this figure.

profiling of ChAT-eGFP$^+$ and ChAT-eGFP$^-$ macrophages isolated from cold-exposed IWAT. RNA sequencing (RNA-seq) revealed robust up-regulation of genes necessary for acetylcholine synthesis and secretion (Figs 1K and L, and EV2J). Pathway analysis revealed an enrichment of neurotransmitter regulation, cellular proliferation, and adrenergic signaling in ChAT-eGFP$^+$ macrophages (Fig 1M). Together, these data suggest that acetylcholine-synthesizing macrophages, which we term ChAMs (cholinergic adipose macrophages), respond to environmental stimuli and may be important for regulating thermogenic function in subcutaneous fat.

Loss of ChAT in macrophages compromises the adaptive thermogenic capacity of subcutaneous fat

Immune cells have been widely reported as key players in regulating adipose thermogenesis (Brestoff et al, 2015; Kohlgruber et al, 2018; Villarroya et al, 2018; Hu et al, 2020). Having demonstrated that several acetylcholine-secreting immune cell types reside in IWAT and that knockout of ChAT in all hematopoietic cell types compromises adaptive thermogenic capacity (Jun et al, 2018), we sought to identify which are important for driving activation of beige adipocytes.

Given that macrophages, T cells, and B cells together comprise approximately 90% of the ChAT-expressing cell population residing in IWAT (Table EV1), we generated macrophage-specific (ChAT$^{fl/fl}$; LysM-Cre), T-cell-specific (ChAT$^{fl/fl}$;Cd4-Cre), and B-cell-specific (ChAT$^{fl/fl}$;Mb1-Cre) ChAT knockout mice (Fig 2A) and confirmed Chat deletion in sorted cells from IWAT in each model (Figs 2B and EV3A and B). ChAT deficiency in macrophages, T cells, or B cells did not cause abnormalities in body weight and IWAT weight at the basal condition (Fig 2C and D). All three ChAT knockout mouse models showed comparable thermogenic gene expression relative to their littermate control animals at room temperature (Fig 2E–G). Following acute cold exposure, ChAT$^{fl/fl}$;LysM-Cre IWAT exhibited significantly reduced activation of genes involved in orchestrating the thermogenic response, such as Ucp1 and Dio2, which may indicate a role for ChAMs in regulating thermogenic activation (Fig 2E). However, for mice lacking ChAT in T cells (ChAT$^{fl/fl}$;Cd4-Cre) or B cells (ChAT$^{fl/fl}$;Mb1-Cre), thermogenic gene activation in IWAT was uncompromised during the response to acute cold exposure (Fig 2F and G).

We further examined the physiological significance of ChAMs in IWAT and at the whole-body level. A cold-induced increase in acetylcholine secretion was observed in IWAT SVF cells of ChAT$^{fl/fl}$ control mice, whereas it was completely absent in those of ChAT$^{fl/fl}$; LysM-Cre mice (Fig 2H). Likewise, UCP1 protein was detected by Western blotting in IWAT of ChAT$^{fl/fl}$ control mice after cold exposure, in contrast to the absence seen in IWAT of ChAT$^{fl/fl}$;LysM-Cre mice (Fig 2I). At the functional level, ChAT$^{fl/fl}$;LysM-Cre IWAT showed a lower oxygen consumption rate (OCR) than control IWAT following cold stimulation (Fig 2J). The thermogenic defects in subcutaneous fat were linked to blunted induction in whole-body OCR and energy expenditure of ChAT$^{fl/fl}$;LysM-Cre mice during acute cold (Figs 2K and EV3C and D). Macrophage-specific ChAT deletion did not affect thermogenic activity of other key thermogenic organs such as BAT or skeletal muscle upon cold exposure (Figs 2L and EV3E and F). Mice lacking ChAT in T cells (ChAT$^{fl/fl}$;Cd4-Cre) or B cells (ChAT$^{fl/fl}$;Mb1-Cre) did not show differences in

cold-induced transcriptional activation of thermogenic genes in BAT compared with littermate control animals (Fig EV3G and H). These results point toward a functional role of ChAMs in sensing thermogenic cues and regulating beige thermogenesis.

ChAMs link adrenergic signaling to beige fat activation

Energy expenditure by white adipose tissue is in part dependent upon adrenergic signaling mediated by catecholamines such as NE (Chouchani & Kajimura, 2019). Initial reports of adipose macrophages synthesizing catecholamines to drive thermogenic activation (Nguyen et al, 2011) have since been refuted (Camell et al, 2017; Fischer et al, 2017; Pirzgalska et al, 2017). We have previously shown that cholinergic immune cells residing in IWAT secrete acetylcholine to communicate with and sustain beige adipocytes via CHRNA2 (Jun et al, 2018), and now have evidence to suggest that ChAMs are the important acetylcholine-secreting cell type in this circuitry.

We sought to investigate how ChAM activity is regulated and found that ChAT-eGFP reporter mice lacking the genes encoding all three β-adrenergic receptors (β-ARs; Adrb1/2/3), termed β-less mice, did not exhibit an increase in IWAT ChAT-eGFP$^+$ cells following acute cold exposure like wild-type (WT) ChAT-eGFP mice do— nor did we observe an increase in the ChAT-eGFP$^+$ macrophage subpopulation (Fig 3A–D). Given the impaired thermoregulatory capacity of β-less mice, these acute cold exposure studies were performed at 10°C instead of 4°C to permit survival. These results suggest that non-neuronal cholinergic activation in IWAT is dependent upon adrenergic signaling. Like in the response to acute cold exposure, ChAT-eGFP mice treated with the pan β-AR agonist NE exhibited significant increases in their total ChAT-eGFP$^+$ population and ChAT $^+$ macrophages within IWAT (Fig 3E and F).

It has been previously reported that tamoxifen-inducible Cx3cr1^{CreER} mice display increased Cre activity in bone marrow-derived circulating myeloid cells compared with tissue-resident myeloid cell types (Yona et al, 2013). Indeed, we observed preferential RFP$^+$ labeling by Cx3cr1^{CreER} in monocyte-derived macrophages compared with resident Kupffer cells in the livers of ChAT-eGFP; Cx3cr1^{CreER}-RFP mice (Figs 3G and H, and EV4A). In the IWAT of this mouse model, less than a quarter of ChAT-eGFP$^+$ macrophages were labeled RFP$^+$ by Cx3cr1^{CreER} following tamoxifen injection (Fig 3I), suggesting a minor contribution from circulating myeloid cells toward IWAT ChAT-eGFP$^+$ macrophages.

Having observed that ChAT-eGFP$^+$ macrophages are responsive to treatment with the pan β-AR agonist NE, we assessed the expression of β-AR genes Adrb1, Adrb2, and Adrb3 by qPCR in primary IWAT macrophages isolated by fluorescence-activated cell sorting (FACS), and found that Adrb2 showed much higher expression than the other β-AR genes (Fig 3J). Likewise, bone marrow-derived macrophages (BMDMs) showed a similar expression pattern to IWAT macrophages, with Adrb2 (encoding the β$_2$-AR) exhibiting the highest relative expression (Fig 3K). Further, flow cytometric analyses of BMDMs detected a subpopulation of ChAT-eGFP$^+$ BMDMs (Fig EV4B), indicating their utility as a system for studying mechanisms of ChAT signaling in macrophages. Treatment of BMDMs with NE for 2 h increased Chat mRNA levels significantly (Fig 3L), and using flow cytometry, we observed an increase in ChAT-eGFP$^+$ cells following NE treatment (Figs 3M and EV4C).
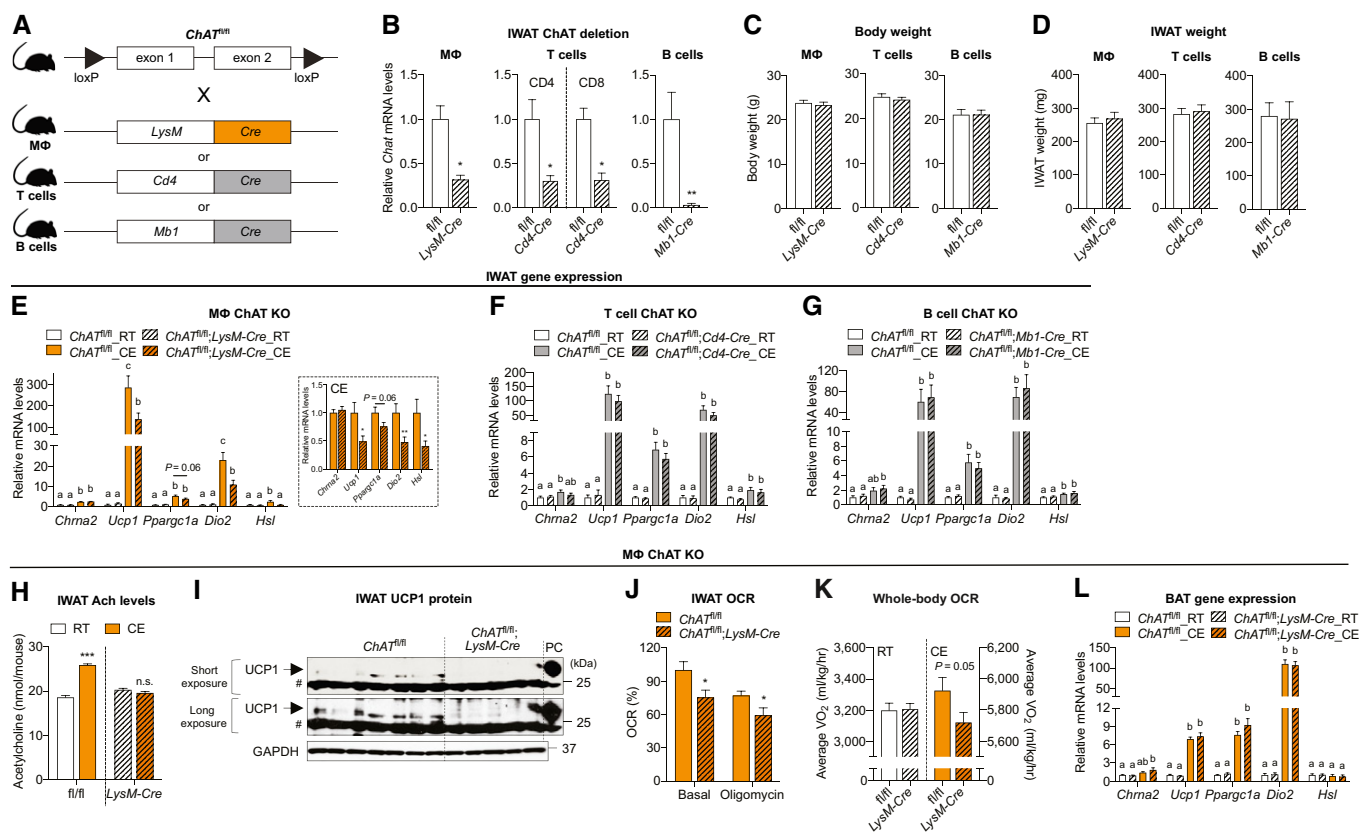
Figure 2. Loss of ChAT in macrophages compromises the adaptive thermogenic capacity of subcutaneous fat.

A   Cell-specific deletion of *ChAT* was achieved by crossing *ChAT*fl/fl mice with *LysM-Cre* (MΦ), *Cd4-Cre* (T cells), or *Mb1-Cre* (B cells) mice.

B   *ChAT* deletion was confirmed in MΦ, CD4+ and CD8+ T cells, and B cells sorted from IWAT of *ChAT*fl/fl;*LysM-Cre* (*n* = 3), *ChAT*fl/fl;*Cd4-Cre* (*n* = 4 for *ChAT*fl/fl, *n* = 3 for *Cre* for CD4, *n* = 4 for CD8), and *ChAT*fl/fl;*Mb1-Cre* mice (*n* = 5 for *ChAT*fl/fl and *n* = 6 for *Cre*), respectively.

C, D   Body weight (C) and IWAT weight (D) of *ChAT*fl/fl;*LysM-Cre* (*n* = 7 for *ChAT*fl/fl, *n* = 8 for *Cre* in C, D), *ChAT*fl/fl;*Cd4-Cre* (*n* = 6 for *ChAT*fl/fl and *n* = 7 for *Cre* in C, D), *ChAT*fl/fl;*Mb1-Cre* (*n* = 12 in C, *n* = 9 for *ChAT*fl/fl, *n* = 8 for *Cre* in D), and littermate *ChAT*fl/fl mice housed at RT.

E–G   mRNA expression of *Chrna2* and thermogenic genes in IWAT of *ChAT*fl/fl;*LysM-Cre* (*n* = 24 for *ChAT*fl/fl_RT, *n* = 25 for *Cre*_RT, *n* = 20 for *ChAT*fl/fl_CE, *n* = 20 for *Cre*_CE) (E), *ChAT*fl/fl;*Cd4-Cre* (*n* = 17 for *ChAT*fl/fl _RT, *n* = 22-23 for *Cre*_RT, *n* = 19 for *ChAT*fl/fl_CE, *n* = 22 for *Cre*_CE) (F), *ChAT*fl/fl;*Mb1-Cre* (*n* = 10 for *ChAT*fl/fl _RT, *n* = 11 for *Cre*_RT, *n* = 9-12 for *ChAT*fl/fl_CE, *n* = 13 for *Cre*_CE) (G), and littermate *ChAT*fl/fl mice housed at RT or 4°C (CE) for 6 h. An insert graph in (E) highlights mRNA expression of *Chrna2* and thermogenic genes in IWAT of *ChAT*fl/fl and *ChAT*fl/fl;*LysM-Cre* mice after 6 h CE.

H   LC/MS-MS was used to quantify Ach secretion from IWAT SVF cells isolated from *ChAT*fl/fl and *ChAT*fl/fl;*LysM-Cre* mice housed at RT or 4 h CE (*n* = 3). n.s.: not significant.

I   Immunoblotting for UCP1 and GAPDH (loading control) in IWAT from *ChAT*fl/fl (*n* = 7) and *ChAT*fl/fl;*LysM-Cre* (*n* = 5) mice after 6 h CE. BAT served as a positive control (PC) for UCP1 expression. Film was subjected to a short and long exposure, and size (kDa) is marked on the right-hand side. #: non-specific bands.

J   Basal and oligomycin-insensitive OCR of IWAT from cold-exposed *ChAT*fl/fl (*n* = 11) and *ChAT*fl/fl;*LysM-Cre* (*n* = 13) mice for 6 h.

K   Average whole-body oxygen consumption rate (OCR) of *ChAT*fl/fl (*n* = 10) and *ChAT*fl/fl;*LysM-Cre* (*n* = 14) mice housed in metabolic chambers at RT or CE for 6 h (from 9 a.m. to 3 p.m.).

L   Relative mRNA expression of *Chrna2* and thermogenic genes in BAT of *ChAT*fl/fl and *ChAT*fl/fl;*LysM-Cre* mice housed at RT or 6 h CE (*n* = 12 for *ChAT*fl/fl_RT, *n* = 13 for *ChAT*fl/fl;*LysM-Cre*_RT, *n* = 15 for *ChAT*fl/fl_CE, *n* = 14 for *ChAT*fl/fl;*LysM-Cre*_CE).

Data information: For (B, E–G and L), mRNA expression was measured by qPCR and normalized to levels of *Tbp* using the $2^{-\Delta\Delta Ct}$ method. In (B-E, H and J–K), data are presented as mean ± SEM where *$P < 0.05$, **$P < 0.01$, and ***$P < 0.001$ (two-tailed Student's *t*-test). In (E–G and L), data are presented as mean ± SEM and the letters "a", "b", and "c" indicate $P < 0.05$ between groups (one-way ANOVA).

Source data are available online for this figure.

However, no increase was detected in β-less ChAT-eGFP BMDMs. These data suggest that adrenergic signaling may be integral in regulating the function of acetylcholine-synthesizing macrophages.

ChAMs function selectively via activation of the β₂-AR

Hematopoietic cells express adrenergic receptors and respond to catecholamines for developmental and functional regulation (Muthu *et al*, 2007; Scanzano & Cosentino, 2015). Having shown that ChAM activity relies upon β-AR activation in IWAT, we sought to determine which receptor(s) is/are crucial for regulating the cholinergic function of these cells. To test this *in vivo*, we treated ChAT-eGFP mice with pharmacological agonists for the β₁-AR (dobutamine), β₂-AR (formoterol), and β₃-AR (CL 316,243). Only treatment with the β₂-AR agonist resulted in increased total ChAT-eGFP+ cells and ChAMs within IWAT (Fig 4A–C). There were no changes in the
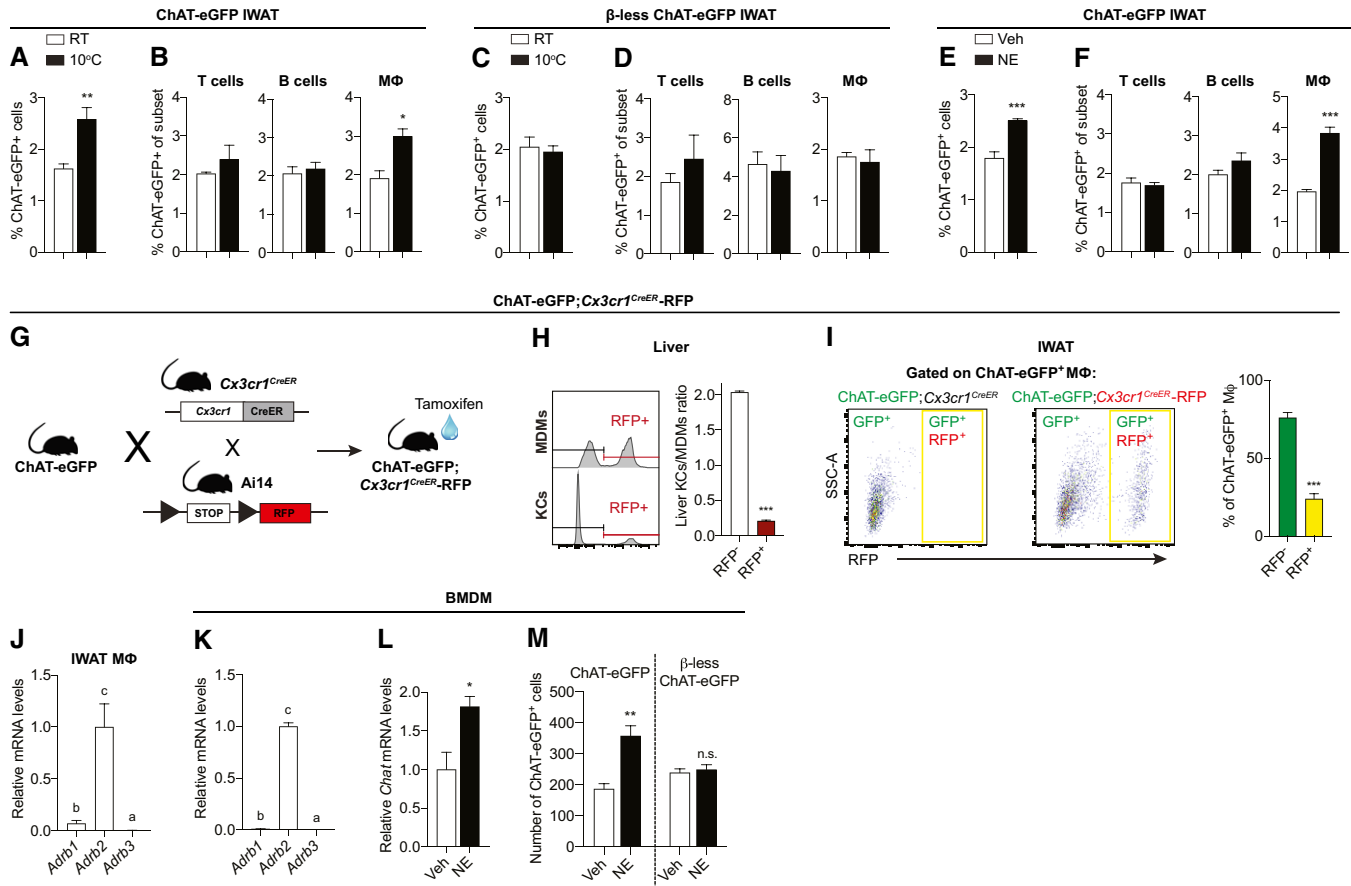
Figure 3. ChAMs link adrenergic signaling to beige fat activation.

A ChAT-eGFP⁺ cells as a percentage of total IWAT SVF cells from ChAT-eGFP mice housed at RT ($n = 7$) or 10°C for 4 h ($n = 3$).

B Percentages of total T cells, B cells, and MΦ that are ChAT-eGFP⁺ in IWAT from ChAT-eGFP mice housed at RT ($n = 7$) or 10°C for 4 h ($n = 3$).

C ChAT-eGFP⁺ cells as a percentage of total IWAT SVF cells from β-less ChAT-eGFP mice housed at RT or 10°C for 4 h ($n = 4$).

D Percentages of total T cells, B cells, and MΦ that are ChAT-eGFP⁺ in IWAT from β-less ChAT-eGFP mice housed at RT or 10°C for 4 h ($n = 4$).

E ChAT-eGFP⁺ cells as a percentage of total IWAT SVF cells from ChAT-eGFP mice treated with vehicle (veh) or 1 mg/kg NE for 2 h ($n = 6$).

F Percentages of total T cells, B cells, and MΦ that are ChAT-eGFP⁺ in IWAT from ChAT-eGFP mice treated with veh or 1 mg/kg NE for 2 h ($n = 6$).

G Schematic describing the generation of ChAT-eGFP;$Cx3cr1^{CreER}$-RFP mice by crossing ChAT-eGFP, $Cx3cr1^{CreER}$, and Ai14 animals.

H Left: Representative histograms showing RFP expression profile of liver monocyte-derived MΦ (MDMs) and Kupffer cells (KCs) in ChAT-eGFP;$Cx3cr1^{CreER}$-RFP mice. Right: Ratio of liver KCs to MDMs that are labeled RFP⁻ or RFP⁺ in ChAT-eGFP;$Cx3cr1^{CreER}$-RFP mice ($n = 3$).

I Left: Representative flow plots showing ChAT-eGFP⁺ and $Cx3cr1^{CreER}$-RFP⁺ double-positive MΦ (yellow gate) in the IWAT of ChAT-eGFP;$Cx3cr1^{CreER}$-RFP mice. Right: Percentage of ChAT-eGFP⁺ MΦ that are RFP⁻ or RFP⁺ in the IWAT of ChAT-eGFP;$Cx3cr1^{CreER}$-RFP mice ($n = 5$).

J Relative mRNA expression of $Adrb1$, $Adrb2$, and $Adrb3$ in IWAT MΦ sorted from WT mice ($n = 4$). Expression was measured by qPCR and normalized to levels of Tbp using the $2^{-\Delta\Delta Ct}$ method.

K Relative mRNA expression of $Adrb1$, $Adrb2$, and $Adrb3$ in BMDMs ($n = 3$). mRNA expression was measured by qPCR and normalized to levels of Tbp using the $2^{-\Delta\Delta Ct}$ method.

L Relative mRNA expression of $Chat$ in BMDMs treated for 2 h with veh or 100 μM NE ($n = 6$). mRNA expression was measured by qPCR and normalized to levels of Tbp using the $2^{-\Delta\Delta Ct}$ method.

M Total number of ChAT-eGFP⁺ cells in BMDMs derived from ChAT-eGFP and β-less ChAT-eGFP mice ($n = 4$). BMDMs were treated for 2 h with veh or 100 μM NE; then, an equal number of events (50,000) were analyzed by flow cytometry. n.s., not significant.

Data information: In (A–F, H–I and L–M), data are presented as mean ± SEM where *$P < 0.05$, **$P < 0.01$, and ***$P < 0.001$ (two-tailed Student's t-test). In (J–K), data are presented as mean ± SEM and the letters "a", "b", and "c" indicate $P < 0.05$ between groups (one-way ANOVA).

Source data are available online for this figure.

ChAT-eGFP⁺ lymphocyte subpopulations following any treatment. The increase in ChAT-eGFP⁺ cells and ChAMs was not observed in β-less mice treated with β₂-AR agonist, nor did we detect any changes in total ChAT-eGFP⁺ cells or immune subsets in BAT following β₂-AR activation (Fig EV5A–D). These results correspond to the high expression of $Adrb2$ seen in IWAT macrophages, and likewise in BMDMs (Fig 3J and K).

We then sought to assess adrenergic activation of ChAT⁺ cells using genetic deletion models. ChAT-eGFP reporter mice with genetic knockout combinations of β-ARs 1-3 were administered with

NE and their ChAT-eGFP⁺ IWAT SVF cells analyzed by flow cytometry (Fig 4D and E). Total ChAT-eGFP⁺ cells and ChAT⁺ macrophages were both increased by treatment with NE in ChAT-eGFP mice with all β-AR genes intact. Likewise, ChAT-eGFP mice lacking β-ARs 1 and 3 ($β_2$WT) also exhibited elevated ChAT-eGFP⁺ cells and cholinergic macrophages after NE. However, genetic deletion of the $β_2$-AR ($β_2$KO) eliminated the activation of cholinergic cells, namely macrophages. Acetylcholine secretion was elevated when $β_2$WT IWAT

Figure 4.
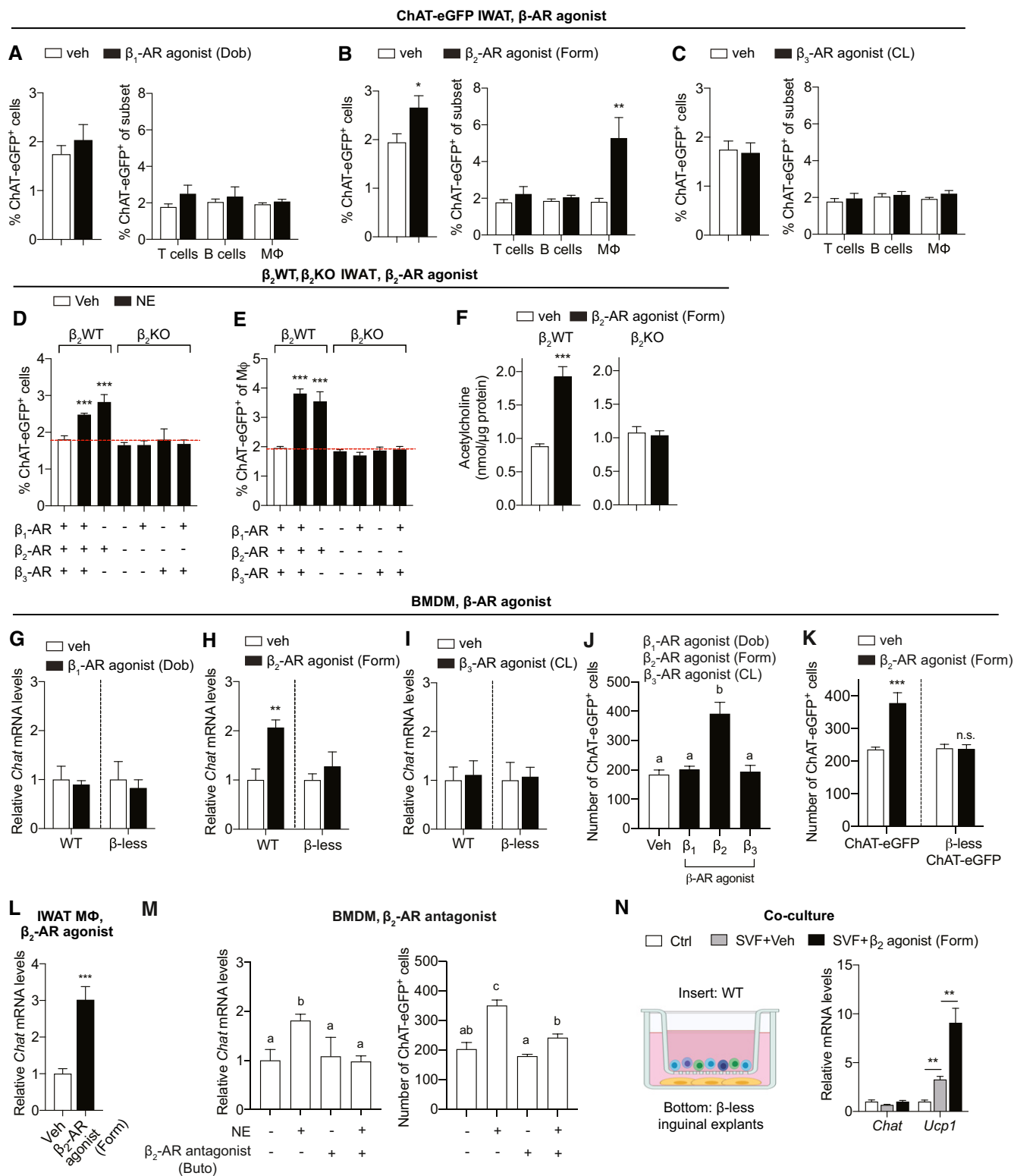
Figure 4. ChAMs function selectively via activation of the β₂-AR.

A–C ChAT-eGFP mice were treated with (A) veh ($n = 4$) or β₁-AR agonist (1 mg/kg dobutamine, Dob) ($n = 3$), (B) veh ($n = 7$) or β₂-AR agonist (1 mg/kg formoterol, Form) ($n = 7$), or (C) veh ($n = 4$) or β₃-AR agonist (1 mg/kg CL 316,243, CL) ($n = 4$ for MΦ; $n = 3$ for T cells and B cells) for 4 h, and the percentages of total IWAT SVF cells and of total T cells, B cells, and MΦ that were ChAT-eGFP⁺ were measured by flow cytometry.

D, E Percentage of (D) total IWAT SVF cells and (E) IWAT MΦ-expressing ChAT-eGFP in reporter mice with genetic deletion combinations of β-ARs 1, 2, and 3 following treatment with veh (white bar: $n = 7$) or 1 mg/kg NE (black bars: from left to right, $n = 7, 5, 4, 5, 4, 7$) for 2 h.

F LC/MS-MS quantification of acetylcholine levels secreted by SVF cells derived from IWAT of β₂WT and β₂KO mice treated with veh or 1 mg/kg Form for 2 h ($n = 3$).

G–I BMDMs were isolated and grown from WT and β-less mice then treated for 2 h with (G) veh ($n = 6$ WT, $n = 6$ β-less) or β₁-AR agonist (2.5 μM Dob) ($n = 6$ WT, $n = 6$ β-less), (H) veh ($n = 6$ WT, $n = 4$ β-less) or β₂-AR agonist (2.5 μM Form) ($n = 6$ WT, $n = 4$ β-less), or (I) veh ($n = 6$ WT, $n = 6$ β-less) or β₃-AR agonist (2.5 μM CL) ($n = 5$ WT, $n = 6$ β-less). *Chat* mRNA expression was measured by qPCR and normalized to levels of *Tbp* using the $2^{-\Delta\Delta Ct}$ method.

J Total number of ChAT-eGFP⁺ cells in BMDMs derived from ChAT-eGFP mice. BMDMs were treated for 2 h with veh or β₁-AR agonist (2.5 μM Dob), β₂-AR agonist (2.5 μM Form), or β₃-AR agonist (2.5 μM CL); then, an equal number of events (50,000) were analyzed by flow cytometry ($n = 4$).

K Total number of ChAT-eGFP⁺ cells in BMDMs derived from ChAT-eGFP and β-less ChAT-eGFP mice. BMDMs were treated for 2 h with veh or β₂-AR agonist (2.5 μM Form); then, an equal number of events (50,000) were analyzed by flow cytometry ($n = 4$). n.s: not significant.

L Primary MΦ were isolated from IWAT by FACS, then seeded into cell culture plates and treated for 2 h with veh ($n = 6$) or β₂-AR agonist (2.5 μM Form) ($n = 4$). *Chat* mRNA expression was measured by qPCR and normalized to levels of *Tbp* using the $2^{-\Delta\Delta Ct}$ method.

M Left: BMDMs were treated for 2 h with veh or pan β-AR agonist (100 μM NE), β₂-AR antagonist (5 μM butoxamine, Buto), or a combination of NE and β₂ antagonist (Buto) ($n = 6$). *Chat* mRNA expression was measured by qPCR and normalized to levels of *Tbp* using the $2^{-\Delta\Delta Ct}$ method. Right: Total number of ChAT-eGFP⁺ BMDMs. ChAT-eGFP BMDMs were treated for 2 h with veh or pan β-AR agonist (100 μM NE), β₂-AR antagonist (5 μM butoxamine, Buto) or a combination of NE and β₂-AR antagonist (Buto) ($n = 4$). An equal number of events (50,000) were analyzed by flow cytometry.

N Left: Bicompartmental co-culture system with media alone (Ctrl) or WT SVF cells isolated from IWAT in the upper compartment (transwell insert) and freshly isolated IWAT explants from β-less mice in the lower compartment. Cells were co-cultured for 4 h in the presence or absence of β₂-AR agonist (2.5 μM Form). 150 μM rivastigmine was added to the media to prevent degradation of Ach. Right: qPCR analyses of *Chat* and *Ucp1* mRNA levels in β-less explants following co-culture with media ($n = 4$)-, vehicle ($n = 10$)-, or β₂-AR agonist ($n = 10$)-treated SVF cells. mRNA expression was measured by qPCR and normalized to levels of *Tbp* using the $2^{-\Delta\Delta Ct}$ method.

Data information: In (A–C, F–I, K–L and N), data are presented as mean ± SEM where *$P < 0.05$, **$P < 0.01$, and ***$P < 0.001$ (two-tailed Student's *t*-test). In (D–E), data are presented as mean ± SEM where ***$P < 0.001$ compared with vehicle-treated (two-tailed Student's *t*-test). In (J and M), data are presented as mean ± SEM and the letters "a", "b", and "c" indicate $P < 0.05$ between groups (one-way ANOVA).

Source data are available online for this figure.

SVF cells were treated with the β₂-AR agonist formoterol, whereas this increase was not evident in β₂KO SVF treated with β₂-AR agonist (Fig 4F).

qPCR analyses of WT and β-less BMDMs treated with agonists for β-ARs 1, 2, or 3 showed induction of *Chat* expression only in WT cells following β₂-AR agonist treatment (Figs 4G–I and EV5E and F). This result was confirmed by flow cytometry, where β₂-AR agonist treatment resulted in increased counts of ChAT-eGFP⁺ BMDMs (Figs 4J and EV5G and H). This increase following β₂-AR agonist administration was not evident in β-less BMDMs treated with β₂-AR agonist, however (Figs 4K and EV5I). Treatment of primary sorted IWAT macrophages with β₂-AR agonist also resulted in up-regulation of *Chat* expression (Fig 4L). Induction of *Chat* mRNA expression by NE in WT BMDMs was abolished by pharmacological blockade of the β₂-AR using a β₂-AR-specific antagonist (Fig 4M). The same effect was observed in ChAT-eGFP BMDMs by flow cytometry—the NE-induced increase in ChAT-eGFP⁺ cells was not present following co-treatment of NE with β₂-AR antagonists butoxamine or ICI 118,551 (Figs 4M and EV5J and K).

Differentiation of BMDMs in the presence of minced adipose tissue generates cells that exhibit characteristics of adipose-resident macrophages, termed BM-ATMs (bone marrow–adipose tissue macrophages) (Flaherty *et al*, 2019). A transwell co-culture system was used to generate BM-ATMs, which exhibit a similar expression pattern of *Adrb1*, *Adrb2*, and *Adrb3* to IWAT macrophages (Figs 3J and EV5L). We demonstrated that β₂-AR agonist treatment significantly induces *Chat* expression in BM-ATMs from WT mice but not from β-less mice (Fig EV5L). We then employed another bicompartmental co-culture system to determine whether treatment of IWAT SVF with β₂-AR agonist induced thermogenic gene expression in adipose explants. IWAT explants were seeded in wells then media,

vehicle-treated or β₂-AR agonist-treated SVF cells were seeded into permeable transwells with 0.4 μm pores to allow diffusion of molecules but not cells (Fig 4N). Explants were taken from β-less mice to prevent unintended activation from the pharmacological β₂-AR agonist used to treat SVF cells. As we have shown previously with differentiated preadipocytes (Jun *et al*, 2018), co-culture of SVF induced *Ucp1* expression in IWAT explants, with no induction seen in the absence of SVF cells. Further, co-culture of SVF cells treated with β₂-AR agonist resulted in significantly higher *Ucp1* induction. However, when SVF from β₂KO IWAT was used, no increase in *Ucp1* expression was observed following treatment with β₂-AR agonist (Fig EV5M). Likewise, with SVF from *ChAT*^fl/fl;*LysM-Cre* IWAT (the absence of macrophage-derived acetylcholine), *Ucp1* was not induced in either treatment condition when compared to the absence of SVF altogether. These results demonstrate that ChAM function is regulated selectively via the β₂-AR and that ChAM activation can induce thermogenic gene expression in IWAT, pointing toward a role in the physiological regulation of thermogenesis.

Discussion

Our investigations have uncovered a discrete population of cholinergic macrophages (ChAMs) that reside in subcutaneous adipose tissue. These cells secrete acetylcholine to regulate the activation of thermogenic adipocytes, and their activity is controlled via adrenergic signaling through the β₂-AR. Loss-of-function studies in mice demonstrated that macrophages are essential for the cholinergic regulation of adaptive thermogenesis, whereas acetylcholine-synthesizing lymphocytes were dispensable for this function. We revealed that ChAMs are dependent specifically upon β₂-AR

activation to induce acetylcholine secretion, using a combination of pharmacological and genetic approaches. These findings elucidate the cellular and molecular mechanisms underlying a novel immune and adipocyte circuitry previously discovered by our group (Jun *et al*, 2018), and affirm the importance of macrophages in regulating adipose tissue function.

Previous reports suggesting that adipose tissue macrophages can produce catecholamines (Nguyen *et al*, 2011) were later refuted due to the absence of tyrosine hydroxylase, the enzyme responsible for catecholamine biosynthesis, in these cells (Camell *et al*, 2017; Fischer *et al*, 2017; Pirzgalska *et al*, 2017). Here, we have clearly shown the presence of ChAT in macrophages using two separate reporter mouse strains and demonstrated that these cells synthesize and secrete acetylcholine. As part of the acute response to cold exposure, acetylcholine secretion was induced within subcutaneous fat. Given our previous finding that several adipose-resident immune cell types express ChAT (Jun *et al*, 2018), it was not surprising that cell-specific deletion of ChAT in macrophages did not fully ablate basal acetylcholine secretion. Importantly, however, here we demonstrated that macrophages are essential for the cold-induced secretion of acetylcholine that forms the basis of this pathway's role in driving adaptive thermogenesis. This was attested to by loss-of-function models, where macrophage-specific ChAT deletion impaired thermogenic capacity in response to cold, whereas deletion of ChAT in T cells and B cells did not compromise cold-induced thermogenic activation. Given that cholinergic lymphocytes have been implicated in regulating local innate immunity, inflammation, and viral defense (Rosas-Ballina *et al*, 2011; Reardon *et al*, 2013; Cox *et al*, 2019) in other tissues, it is plausible that their counterparts in adipose tissue carry out corresponding functions, separate from regulating thermogenesis.

We have functionally characterized this new population of adipose macrophages, with transcriptomic profiling demonstrating that ChAMs are dedicated to neurotransmitter regulation and highly enriched for acetylcholine signaling genes and pathways. A distinct functional niche for acetylcholine-synthesizing cells is not unprecedented, given that ChAT-expressing CD4 T cells have been described as a unique lymphocyte subset responsible for blood pressure regulation (Olofsson *et al*, 2016). Significant advances have been made in recent years regarding our understanding of functionally distinct macrophage subpopulations in fat—in particular within the obese and thermogenic adipose microenvironment (Pirzgalska *et al*, 2017; Hill *et al*, 2018; Chakarov *et al*, 2019; Jaitin *et al*, 2019; Knights *et al*, 2020a) (Fig EV2M–R). Given this inherent heterogeneity in tissue macrophages, future investigations will further reveal how cholinergic macrophages and other subsets fit into the functional milieu of resident immune cells—particularly in subcutaneous fat. For example, further studies will help to elucidate how ChAMs fit into the broader classification of adipose macrophages, and what hallmarks of the M1-M2 spectrum they might possess. β_2-AR signaling has been reported to play a role in polarizing macrophages toward an M2-like phenotype (Grailer *et al*, 2014), although not via conventional STAT6-mediated mechanisms (Lamkin *et al*, 2016). In addition to the well-characterized role of β_3-AR-mediated signaling in thermogenic activation of adipocytes, studies have shown that β_2-AR signaling can also directly promote beige adipocyte development (Ohyama *et al*, 2016). Headway is currently being made that aims to harness cholinergic signaling pathways as a therapy for metabolic

diseases such as obesity and type 2 diabetes, and our findings reveal potential new therapeutic avenues for investigation.

In addition to their communication with beige adipocytes, it will be imperative to better understand the other cell types that ChAMs may interact with in the thermogenic niche, such as $\gamma\delta$ T cells, which have recently come to prominence in thermogenic regulation (Kohlgruber *et al*, 2018; Hu *et al*, 2020), and whether acetylcholine secretion from ChAMs plays additional roles in adipose homeostasis besides driving adaptive thermogenesis. Beyond adipose tissue, it is conceivable that homologous non-neuronal cholinergic circuitry exists in other metabolic tissues such as the liver, just as immune cells in the spleen secrete acetylcholine to regulate inflammation (Rosas-Ballina *et al*, 2011). Given the beneficial role that ChAMs play in regulating adaptive thermogenesis, manipulating non-neuronal cholinergic circuitry represents a promising avenue for therapeutic intervention to increase energy expenditure and improve metabolic ailments.

Materials and Methods

Reagents

Rivastigmine tartrate (129101-54-8) was purchased from Cayman Chemical. (−)-Norepinephrine (A7257), CL 316,243 hydrate (C5976), R(−)-denopamine (D7815), oligomycin (75351), tamoxifen (T5648), and OptiPrep Density Gradient Medium (D1556) were purchased from Sigma. Butoxamine hydrochloride (sc-234233), dobutamine hydrochloride (sc-203031), formoterol fumarate (sc-203050), and terbutaline hemisulfate (sc-213000) were purchased from Santa Cruz. Collagenase D (11088882001), collagenase B (11088831001), and dispase II (04942078001) were purchased from Roche. ICI 118,551 hydrochloride (0821) was purchased from Tocris. DMEM/F-12 GlutaMAX (10565-042) was purchased from Life Technologies.

Mice

Animal studies were undertaken in accordance with the protocol reviewed and approved by the Institutional Animal Care and Use Committee at the University of Michigan. Mice were exposed to a 12-h light/dark cycle and fed standard rodent chow (5L0D; PicoLab) unless otherwise specified, where mice were fed a high-fat diet (D12451; Research Diets) in which fat comprised 45% of calories. Throughout, mice were age-matched and then randomly assigned to treatment groups to minimize the effects of subjective bias. ChAT-eGFP, *ChAT-Cre*, Ai14, *ChAT*^fl/fl^, *Vav-iCre*, *LysM-Cre*, *Cd4-Cre*, *Mb1-Cre*, and *Cx3cr1-CreER* mice were all obtained from the Jackson Laboratories (stock nos. 007902, 031661, 007914, 016920, 008610, 004781, 022071, 020505, and 020940, respectively). ChAT double reporter mice were generated by crossing ChAT-eGFP mice with *ChAT-Cre* and Ai14 reporter mice. *ChAT*^fl/fl^ mice were crossed with *Vav-iCre*, *LysM-Cre*, *Cd4-Cre*, or *Mb1-Cre* animals to generate cell-specific knockout of *ChAT* in hematopoietic cells (*ChAT*^fl/fl^;*Vav-iCre*), macrophages (*ChAT*^fl/fl^; *LysM-Cre*), T cells (*ChAT*^fl/fl^;*Cd4-Cre*), or B cells (*ChAT*^fl/fl^;*Mb1-Cre*), respectively. *Vav-iCre* and *LysM-Cre* mice were crossed with Ai14 mice and ChAT-eGFP mice to profile the efficiency and cell specificity of these constitutive Cre models.

ChAT-eGFP mice were crossed with *Cx3cr1-CreER* and Ai14 animals to generate ChAT-eGFP mice with the capacity for inducible labeling of *Cx3cr1*-expressing myeloid cell types. To induce Cre activity, mice were administered for 5 days with 5 mg of tamoxifen by oral gavage, then rested for 7 days before experimentation. β-less mice, lacking *Adrb1, Adrb2,* and *Adrb3,* were kindly provided by Brad Lowell (Beth Israel Deaconess Medical Center, Boston). Combinations of β_1-, β_2-, and β_3-AR knockouts containing the ChAT-eGFP reporter were generated by crossing β-less mice with ChAT-eGFP mice. Age-matched male and female mice (6–10 weeks old) were used for cold exposure, genetic, and pharmacological β-AR experiments. In cold exposure experiments, mice were singly housed in pre-chilled cages inside an environmental chamber at 10°C or 4°C. For β-AR studies, mice were injected I.P. with 1 mg/kg NE for 2 h, or subjected to 4 h treatment with 1 mg/kg dobutamine (β_1-AR agonist), formoterol (β_2-AR agonist), or CL 316,243 (β_3-AR agonist). Core body temperature of *ChAT*$^{fl/fl}$ and *ChAT*$^{fl/fl}$;*LysM-Cre* mice housed at room temperature or 6 h cold was monitored using a RET-3 mouse rectal probe (World Precision Instruments).

Metabolic phenotyping

Systemic energy metabolism of *ChAT*$^{fl/fl}$ and *ChAT*$^{fl/fl}$;*LysM-Cre* mice was evaluated using the Comprehensive Laboratory Animal Monitoring System (CLAMS, Columbus Instruments) by the University of Michigan Animal Phenotyping Core. Mice were acclimated in metabolic chambers, and their whole-body oxygen consumption (VO_2), energy expenditure (VO_2, VCO_2), and locomotor activity (beam break counts) were monitored at room temperature or 4°C for 6 h (from 9 a.m. to 3 p.m.). Whole-body oxygen consumption and energy expenditure over 6 h were corrected by lean body mass.

Tissue oxygen consumption rate

ChAT$^{fl/fl}$ and *ChAT*$^{fl/fl}$;*LysM-Cre* mice were kept at 4°C for 6 h and treated with 1 mg/kg formoterol for 30 min to amplify β_2-AR-dependent ChAT signaling. Isolated IWAT from the cold-exposed mice was weighed and minced in respiration buffer (2.5 mM glucose, 50 μM palmitoyl-L-carnitine hydrochloride, 2.5 mM malate, 120 mM NaCl, 4.5 mM KCl, 0.7 mM Na_2HPO_4, 1.5 mM NaH_2PO_4, and 0.5 mM $MgCl_2$, pH 7.4). Oxygen consumption was recorded at the basal or uncoupled stage with 4 mg/ml oligomycin using a Clark electrode (Strathkelvin Instruments) and normalized with IWAT weight.

Primary cell culture

BMDMs were cultured based on previously performed protocols (Knights *et al*, 2016; Knights *et al*, 2020b; Zhu *et al*, 2020). Briefly, femora and tibiae were extracted from 6 to 10 week old mice, flushed, and subjected to red blood cell lysis. Cells were grown on non-tissue culture-treated sterile petri dishes in 80% v/v DMEM/F-12 GlutaMAX medium supplemented with 20% v/v conditioned medium from L929 cells. After 5–7 days, cells were seeded for experiments. To grow adipose-like BMDMs (BM-ATMs), we replicated a previously published protocol (Flaherty *et al*, 2019). Bone marrow cells were flushed as above; then, non-adherent cells were passaged and allowed to adhere in the presence of minced IWAT

using co-culture transwells (Corning). For co-culture of IWAT SVF cells and IWAT explants, SVF cells were freshly isolated from WT, β_2 KO, or *ChAT*$^{fl/fl}$;*LysM-Cre* mice (the upper compartment) and co-cultured with IWAT explants from β-less mice (the lower compartment) for 4 h in the presence or absence of 2.5 μM formoterol, with 150 μM rivastigmine to prevent acetylcholine breakdown. The IWAT explants were then harvested from the lower compartment to analyze gene expression by qPCR. To culture primary IWAT macrophages, cells were isolated by FACS directly into DMEM/F-12 GlutaMAX culture medium containing 10% fetal bovine serum and 1x penicillin–streptomycin. Sorted macrophages (live CD45$^+$ Ly6G$^-$ SiglecF$^-$ NK1.1$^-$ CD3$^-$ CD19$^-$ CD11b$^+$ CD64$^+$ cells) were seeded at a density of 150,000 cells per well of a 12-well plate. Cells were given 90 min to adhere prior to treatment.

For β-AR studies, cells were treated for 2 h with 2.5 μM denopamine, 2.5 μM dobutamine (β_1-AR agonists), 2.5 μM formoterol, 10 μM terbutaline (β_2-AR agonists), 2.5 μM CL 316,243 (β_3-AR agonist), 100 μM NE (pan β-AR agonist), 5 μM ICI 118,551, or 5 μM butoxamine (β_2-AR antagonists).

Gene expression analysis

Gene expression analysis was performed by standard methods, as previously described (Qiao *et al*, 2019). Total RNA from adipose tissues, skeletal muscle, and cultured cells was isolated by the TRIzol method. Equal amounts of RNA were subjected to cDNA synthesis according to the manufacturer's instructions for the M-MLV Reverse Transcriptase Kit (Invitrogen). qPCRs were performed in 384-well plates and utilized Power SYBR Green Chemistry (Life Technologies). To calculate relative expression levels, the $2^{-\Delta\Delta Ct}$ method was used, with normalization to expression of the TATA box-binding protein (*Tbp*) housekeeping gene. All primer sequences can be found in Table EV2.

Immunoblotting

Total protein was extracted from IWAT of acute cold-exposed *ChAT*$^{fl/fl}$ and *ChAT*$^{fl/fl}$;*LysM-Cre* mice using ice-cold RIPA buffer (50 mM Tris–HCl, pH 7.5, 1% Triton X-100, 1% sodium deoxycholate, 0.1% SDS, 150 mM NaCl, and 1 mM phenylmethylsulfonyl fluoride) supplemented with a protease inhibitor cocktail (Roche) and phosphatase inhibitors (10 mM NaF, 60 mM β-glycerolphosphate, pH 7.5, 2 mM sodium orthovanadate, and 10 mM sodium pyrophosphate). We loaded 125 μg of IWAT protein onto SDS–PAGE and subsequently transferred the protein onto PVDF membranes. The membranes were incubated with antibodies against UCP1 (Abcam, #ab10983) and GAPDH (Cell Signaling, #5174).

Tissue isolation and digestion

Adipose tissue was harvested from the inguinal subcutaneous depot (IWAT), visceral gonadal depot (VWAT), or the interscapular brown depot (BAT). SVF cells were isolated from IWAT, VWAT, or BAT by collagenase digestion as described previously (Jun *et al*, 2018). Briefly, depots were dissected, minced, and digested in a collagenase solution (1.5 U/ml) (collagenase D for IWAT and VWAT, and collagenase B for BAT) and dispase II (2.4 U/ml) supplemented with 10 mM $CaCl_2$ for 20 min in a 37°C water bath with agitation.

Digested tissues were washed with PBS and filtered through a 100-μm strainer, and the filtrate was centrifuged at 500 *g* for 5 min to pellet SVF cells and remove the floating adipocyte layer. For lymph node studies, the inguinal lymph node was microdissected and subjected to mincing with a razor blade, then enzymatically digested in a solution comprised of 1.5 U/ml collagenase D and 2.4 U/ml dispase II for 20 min in a 37°C water bath with agitation, followed by washing and centrifugation as for adipose depots.

For liver studies, non-parenchymal cells (NPCs) were isolated using a mechanical digestion method and density-based centrifugation adapted from established protocols (Finlon *et al*, 2019; Xiong *et al*, 2019). Livers were mechanically digested in a 100-μm strainer with FACS buffer (PBS containing 2% fetal bovine serum and 1 mM EDTA). Strained cells were washed in FACS buffer and passed through another 100-μm strainer. To remove hepatocytes, cells were centrifuged twice at 50 *g* for 3 min, retaining the supernatant each time. Supernatant was then centrifuged for 10 min at 500 *g* to pellet non-hepatocytes. The pelleted cells were then subjected to density-based centrifugation using a 1:1 mix of FACS buffer with 50% v/v OptiPrep (Sigma), then topped with a layer of FACS buffer. Centrifugation was performed with brakes off at 1,500 *g* for 20 min. The defined cloudy layer (containing NPCs) was collected and washed in FACS buffer in preparation for downstream application.

Flow cytometry and cell sorting

Isolated SVF cells from adipose tissues or lymph node cells were subjected to red blood cell lysis using ddH$_2$O, then pre-blocked using TruStain FcX PLUS (Biolegend) on ice. Liver NPCs were prepared as above and washed in preparation for antibody staining. BMDMs were lifted using cold PBS containing 5 mM EDTA, then washed and pre-blocked as above. Cold FACS buffer (PBS containing 2% fetal bovine serum and 1 mM EDTA) was used for all washing and staining steps. Following pre-blocking, cells were stained at 4°C for 30 min in darkness with combinations of fluorescently conjugated antibodies that can be found in Table EV3. Dead cells were excluded based on uptake of TO-PRO-3 Iodide (Invitrogen), debris were eliminated using side-scatter area (SSC-A) versus forward scatter area (FSC-A), and doublets were excluded using side-scatter height versus width (SSC-H, SSC-W) and forward scatter height versus width (FSC-H, FSC-W). Fluorescence-minus-one (FMO) controls using tissue-matched cells were employed to establish negative and positive gate positioning, and an open channel (488-nm excitation, 710/50-nm emission) was used to gate out autofluorescence. For endogenous fluorescent reporters (GFP and RFP), WT cells were used for FMO controls. UltraComp eBeads (Invitrogen) were used for single-stained compensation controls. To assess intracellular levels of Ki67 and prevent GFP quenching by ethanol fixation, IWAT SVF cells from ChAT-eGFP mice were fixed and permeabilized using the Cyto-Fast Fix/Perm Buffer Set (Biolegend) according to the manufacturer's instructions, prior to staining with anti-Ki67 or isotype. For fixable viability staining, eFluor 660 (Thermo Fisher) was used.

Flow cytometry was performed using an LSR Fortessa (BD Biosciences), and cell sorting was performed on a FACSAria III (BD Biosciences) with a 100-μm nozzle. Data were acquired with FACSDiva software (BD Biosciences) and analyzed using FlowJo v10.6.1 (TreeStar/BD Biosciences).

Dimensionality reduction

To visualize high-parameter flow cytometric data in two dimensions, dimensionality reduction was performed using the Uniform Manifold Approximation and Projection (UMAP) algorithm via a FlowJo plugin (v2.2) (preprint: McInnes *et al*, 2018). Prior to dimensionality reduction, events defined as ChAT-eGFP$^+$ were downsampled to 75,000 using the DownSample plugin (v3.1). The UMAP algorithm was then applied with the following parameters: Distance Function, Euclidean; Nearest Neighbors, 15; and Minimum Distance, 0.5. All data were analyzed and figures generated in FlowJo v10.6.1.

Bulk RNA sequencing

ChAT-eGFP mice were cold-exposed at 4°C for 4 h; then, SVF cells from IWAT were prepared as above, alongside WT cells for unstained and FMO controls. A BD FACSAria III was primed with RNaseZAP (Invitrogen); then, ChAT-eGFP$^+$ and ChAT-eGFP$^-$ macrophages (defined as live CD45$^+$ NK1.1$^-$ CD3$^-$ CD19$^-$ Ly6G$^-$ SiglecF$^-$ CD11b$^+$ CD64$^+$) were sorted through a 100-μm nozzle directly into NEBNext Lysis Buffer (NEB) containing RNase inhibitor, and snap-frozen in a 100% ethanol dry ice bath. Library preparation was undertaken using the NEBNext Single Cell/Low Input RNA Library Prep Kit (NEB #E6420) according to the manufacturer's instructions. Quality control assessment on prepared libraries was performed using Agilent TapeStation. Paired end (150 bp) sequencing was performed on an Illumina NovaSeq (S4).

Snakemake (Koster & Rahmann, 2012) was used to manage the bioinformatics workflow. Reads were trimmed using CutAdapt v2.3 (Martin, 2011), then were mapped to the reference genome GRCm38 (ENSEMBL), using STAR v2.7.8a (Dobin *et al*, 2013), and assigned count estimates to genes with RSEM v1.3.3 (Li & Dewey, 2011). Alignment options followed ENCODE standards for RNA-seq. FastQC v0.11.8 (Andrews, 2010) was run on .bam files in a post-alignment step, including both aligned and unaligned reads, to ensure data quality. Multiqc v1.7 compiled the results from several of these tools and provided a detailed and comprehensive quality control report (Ewels *et al*, 2016). Library preparation, sequencing, and the bioinformatics pipeline were performed by the Advanced Genomics Core at the University of Michigan. With an FPKM cutoff value of 8.91, we identified 1,426 genes that uniquely express in the ChAT-eGFP$^+$ macrophages relative to the ChAT-eGFP$^-$ macrophages ($P < 0.05$). The selected genes were subjected to biological pathway analysis using Metascape (Zhou *et al*, 2019). To calculate relative gene expression between ChAT-eGFP$^-$ and ChAT-eGFP$^+$ macrophages, a pseudocount of 1 was added to all gene counts (FPKM). Published RNA-seq datasets were procured from the NCBI Gene Expression Omnibus at Accession Series GSE125667 (Chakarov *et al*, 2019) and GSE103847 (Pirzgalska *et al*, 2017), for comparative bioinformatics analyses. In the comparison of our data and GSE125667, genes that had more than 0 read counts in Lyve1^{lo}, Lyve1^{hi} or ChAMs were sorted by their read counts in descending order, and the top 4.3% of genes were selected as highly expressed genes in each population for biological pathway analysis using Metascape. We performed a side-by-side comparison of gene expression profiles of ChAMs and sympathetic neuron-associated macrophages (SAM) using our data and GSE103847. To detect commonly

expressed genes in both ChAMs and SAM, we first excluded genes with 0 read counts in ChAMs or SAM and selected non-significantly differentially expressed genes between the two populations ($P > 0.05$). Commonly or uniquely expressed genes in the populations were used for biological pathway analysis in Metascape database.

Quantification of acetylcholine

IWAT SVF was isolated from $ChAT^{fl/fl}$ and $ChAT^{fl/fl}$;Vav-iCre mice and washed in PBS. SVF was then incubated in PBS supplemented with 150 μM rivastigmine for 30 min at room temperature. After incubation, supernatants were collected following centrifugation and acetylcholine was measured using a previously described approach utilizing liquid chromatography coupled to tandem mass spectrometry (LC-MS/MS) for analyzing neurotransmitters (Song et al, 2012; Jun et al, 2018). Briefly, standard solutions of acetylcholine were prepared in 250 μM ascorbic acid in water to create a calibration range of 0.25–125 nM. Calibration curves were prepared based on the peak area ratio of the standard to the internal standard by linear regression. A deuterium labeled internal standard (d4-acetylcholine; C/D/N isotopes) was added to samples and standards, diluted 1:3 (v/v) in water, and centrifuged for 10 min at 12,100 g. The supernatant was transferred to an HPLC vial and analyzed as described below. All samples and standards were analyzed in triplicate using a Phenomenex Kinetex C18 chromatography column (100 × 2.1 mm, 1.7 μm, 100 Å) on a Vanquish ultrahigh-pressure liquid chromatograph (Thermo Fisher) interfaced to a TSQ Quantum Ultra triple quadrupole mass spectrometer (Thermo Fisher). Mobile phase A was 10 mM ammonium formate with 0.15% (v/v) formic acid in water. Mobile phase B was acetonitrile. The gradient used was as follows: initial, 5% B; 0.60 min, 8% B; 0.68 min, 26% B, 1.05 min, 75% B; 1.8 min, 100% B; 2.2 min, 100% B; 2.2 min, 5% B; and 3.0 min, 5% B at 600 μl/min. The sample injection volume was 5 μl. The autosampler was kept at ambient temperature, and the column was held at 30°C in still air mode. Electrospray ionization was used in positive mode at 4 kV. The capillary temperature was 400°C, the vaporizer temperature was 350°C, the sheath gas was 10, and the auxiliary gas was 5. Acetylcholine ions were detected in MS/MS mode with the following transitions: (acetylcholine) product: 87, precursor: 146; (d4-acetylcholine) product: 91, precursor: 150. Tube lens and collision energy were 53 and 13, respectively. Automated peak integration was performed using XCalibur 3.0 MS software. All peaks were visually inspected to ensure proper integration. To measure cold-induced acetylcholine levels in IWAT SVF from $ChAT^{fl/fl}$ and $ChAT^{fl/fl}$;LysM-Cre animals, mice were housed in pre-chilled cages inside an environmental chamber at 4°C for 4 h. IWAT SVF was isolated and incubated as a single-cell suspension for 30 min in the presence of 150 μM rivastigmine, and then, supernatant was subjected to LC-MS/MS as described above. β_2-AR-dependent acetylcholine secretion was analyzed in IWAT SVF of β_2 WT and β_2 KO mice treated with 1 mg/kg formoterol for 2 h.

Processing and staining for three-dimensional adipose imaging

IWAT from WT and ChAT-eGFP reporter mice was harvested and fixed overnight in 4% paraformaldehyde (PFA) in 1X PBS at 4°C in a conical tube protected from light. Tissues were washed for 1 h three times with 1X PBS at room temperature to remove PFA, then stored at 4°C in 1X PBS with 0.02% sodium azide until processing. Following harvest, fixing, and washing, samples were allocated numbers that concealed their identity before proceeding, allowing processing, staining, and imaging to be performed in a blinded manner by another individual. To maintain overall shape and morphology, each fat pad was situated lying flat in a nylon mesh biopsy pouch and remained there for the duration of the experiment until imaging. Samples were processed with a modified version of the previously published Adipo-clear protocol (Chi et al, 2018) at room temperature on a shaker. Briefly, B1N buffer (0.1% Triton X-100/0.3 M glycine in H_2O, pH 7) and methanol (20/40/60/80/100%) gradient was prepared fresh on the day of the experiment. All tissues were washed for 30 min for each step of the dehydration gradient. Delipidation was completed with dichloromethane (Sigma) washes once for 30 min, followed by once for 60 min. DCM was washed off with two 30-min washes of 100% methanol before completing a reverse gradient to rehydrate (100/80/60/40/20% methanol in B1N buffer) with 20-min washes for each step. Samples were washed in B1N buffer only once for 30 min, followed by 1 h, then overnight in DMSO/Glycine buffer (5% DMSO/ 0.3 M glycine in PTxwH) at 4°C with shaking. The next day, three 1-h washes with PTxwH (0.1% Triton X-100/0.05% Tween 20/2 mg/ml heparin in 1X PBS) were completed at room temperature on a shaker before pooling samples for antibody incubation. All fat tissues were pooled into a single conical and incubated in the minimum amount of PTxwH buffer required to submerge, along with an Alexa Fluor 488-conjugated anti-GFP polyclonal antibody (antibody information can be found in Table EV3) and placed on a room temperature shaker for 4 days. Excess antibody was removed by washing in 1X PBS five times for 1 h.

Index matching and three-dimensional imaging of adipose tissue

Tissues were briefly blotted onto a paper towel to remove excess moisture, then placed in EasyIndex (LifeCanvas Technologies) and incubated overnight at 39°C for index matching. After cooling at room temperature for 3 h, all samples were removed from the nylon mesh pouches and mounted in 1% agarose-EasyIndex onto a sample holder for light-sheet imaging. Samples were imaged immersed in the imaging chamber filled with EasyIndex of the SmartSPIM light-sheet microscope equipped with a 4X objective lens (LifeCanvas Technologies). Images were acquired and stitched using the LifeCanvas SmartSPIM software package. Images were acquired at resolution with a 488-nm laser and a 4-μm z-step. Visualization of 3D images was completed using IMARIS x64 software (Bitplane) in a blinded manner throughout.

Statistical analysis

All results are presented as mean ± standard error of the mean (SEM), depicted in graphs as error bars. GraphPad Prism 8 was used for statistical analyses and generating figures. The Shapiro–Wilk test was used to determine whether data were distributed normally; then, parametric two-tailed Student's t-tests were used to assess statistical significance for two-group comparisons or a one-way analysis of variance (ANOVA) with Tukey's post hoc test for

multiple comparisons involving one independent variable. *P* values are indicated as *P < 0.05, **P < 0.01, and ***P < 0.001 unless otherwise specified. The number of replicates used for calculating statistics can be found in the corresponding legend of each Figure, in addition to Source Data.

Data availability

The RNA sequencing data from this publication have been deposited to the NCBI Gene Expression Omnibus (GEO) database at Accession No. GSE174345 (http://www.ncbi.nlm.nih.gov/geo/query/acc.cgi?acc=GSE174345).

Expanded View for this article is available online.

Author contributions

AJK, HJ, and JW conceived the project and designed the study. AJK, HJ, SL, YM, VSN, EP, MJS, and JW performed the experiments and analyzed the data. RTK, IM, and LY analyzed the data and provided intellectual input. JW oversaw the study. AJK, HJ, SL, and JW wrote the manuscript.

Conflict of interest

The authors declare that they have no conflict of interest.

References

Abram CL, Roberge GL, Hu Y, Lowell CA (2014) Comparative analysis of the efficiency and specificity of myeloid-Cre deleting strains using ROSA-EYFP reporter mice. *J Immunol Methods* 408: 89–100

Amano SU, Cohen JL, Vangala P, Tencerova M, Nicoloro SM, Yawe JC, Shen Y, Czech MP, Aouadi M (2014) Local proliferation of macrophages contributes to obesity-associated adipose tissue inflammation. *Cell Metab* 19: 162–171

Andrews S (2010) FastQC: a quality control tool for high throughput sequence data [Online]. Available online at: http://www.bioinformatics.babraham.ac.uk/projects/fastqc/

Beckmann J, Lips KS (2013) The non-neuronal cholinergic system in health and disease. *Pharmacology* 92: 286–302

Brestoff JR, Kim BS, Saenz SA, Stine RR, Monticelli LA, Sonnenberg GF, Thome JJ, Farber DL, Lutfy K, Seale P *et al* (2015) Group 2 innate lymphoid cells promote beiging of white adipose tissue and limit obesity. *Nature* 519: 242–246

Camell CD, Sander J, Spadaro O, Lee A, Nguyen KY, Wing A, Goldberg EL, Youm Y-H, Brown CW, Elsworth J *et al* (2017) Inflammasome-driven catecholamine catabolism in macrophages blunts lipolysis during ageing. *Nature* 550: 119–123

Chakarov S, Lim HY, Tan L, Lim SY, See P, Lum J, Zhang X-M, Foo S, Nakamizo S, Duan K *et al* (2019) Two distinct interstitial macrophage populations coexist across tissues in specific subtissular niches. *Science* 363: eaau0964

Chi J, Wu Z, Choi CHJ, Nguyen L, Tegegne S, Ackerman SE, Crane A, Marchildon F, Tessier-Lavigne M, Cohen P (2018) Three-dimensional adipose tissue imaging reveals regional variation in beige fat biogenesis and PRDM16-dependent sympathetic neurite density. *Cell Metab* 27: 226–236

Chouchani ET, Kajimura S (2019) Metabolic adaptation and maladaptation in adipose tissue. *Nat Metab* 1: 189–200

Clausen BE, Burkhardt C, Reith W, Renkawitz R, Forster I (1999) Conditional gene targeting in macrophages and granulocytes using LysMcre mice. *Transgenic Res* 8: 265–277

Cox MA, Duncan GS, Lin GHY, Steinberg BE, Yu LX, Brenner D, Buckler LN, Elia AJ, Wakeham AC, Nieman B *et al* (2019) Choline acetyltransferase-expressing T cells are required to control chronic viral infection. *Science* 363: 639–644

Dobin A, Davis CA, Schlesinger F, Drenkow J, Zaleski C, Jha S, Batut P, Chaisson M, Gingeras TR (2013) STAR: ultrafast universal RNA-seq aligner. *Bioinformatics* 29: 15–21

Ewels P, Magnusson M, Lundin S, Kaller M (2016) MultiQC: summarize analysis results for multiple tools and samples in a single report. *Bioinformatics* 32: 3047–3048

Finlon JM, Burchill MA, Tamburini BAJ (2019) Digestion of the murine liver for a flow cytometric analysis of lymphatic endothelial cells. *J Vis Exp* 143: e58621

Fischer K, Ruiz HH, Jhun K, Finan B, Oberlin DJ, van der Heide V, Kalinovich AV, Petrovic N, Wolf Y, Clemmensen C *et al* (2017) Alternatively activated macrophages do not synthesize catecholamines or contribute to adipose tissue adaptive thermogenesis. *Nat Med* 23: 623–630

Flaherty SE 3rd, Grijalva A, Xu X, Ables E, Nomani A, Ferrante Jr AW (2019) A lipase-independent pathway of lipid release and immune modulation by adipocytes. *Science* 363: 989–993

Giordano A, Song CK, Bowers RR, Ehlen JC, Frontini A, Cinti S, Bartness TJ (2006) White adipose tissue lacks significant vagal innervation and immunohistochemical evidence of parasympathetic innervation. *Am J Physiol Regul Integr Comp Physiol* 291: R1243–R1255

Grailer JJ, Haggadone MD, Sarma JV, Zetoune FS, Ward PA (2014) Induction of M2 regulatory macrophages through the beta2-adrenergic receptor with protection during endotoxemia and acute lung injury. *J Innate Immun* 6: 607–618

Hill DA, Lim H-W, Kim YH, Ho WY, Foong YH, Nelson VL, Nguyen HCB, Chegireddy K, Kim J, Habertheuer A *et al* (2018) Distinct macrophage populations direct inflammatory versus physiological changes in adipose tissue. *Proc Natl Acad Sci U S A* 115: E5096–E5105

Hu B, Jin C, Zeng X, Resch JM, Jedrychowski MP, Yang Z, Desai BN, Banks AS, Lowell BB, Mathis D *et al* (2020) gammadelta T cells and adipocyte IL-17RC control fat innervation and thermogenesis. *Nature* 578: 610–614

Jaitin DA, Adlung L, Thaiss CA, Weiner A, Li B, Descamps H, Lundgren P, Bleriot C, Liu Z, Deczkowska A *et al* (2019) Lipid-associated macrophages

control metabolic homeostasis in a Trem2-dependent manner. *Cell* 178: 686−698.e14

Jun H, Yu H, Gong J, Jiang J, Qiao X, Perkey E, Kim D-I, Emont MP, Zestos AG, Cho J-S *et al* (2018) An immune-beige adipocyte communication via nicotinic acetylcholine receptor signaling. *Nat Med* 24: 814−822

Knights AJ, Wu J, Tseng YH (2020a) The heating microenvironment: intercellular cross talk within thermogenic adipose tissue. *Diabetes* 69: 1599−1604

Knights AJ, Yang L, Shah M, Norton LJ, Green GS, Stout ES, Vohralik EJ, Crossley M, Quinlan KGR (2020b) Krüppel-like factor 3 (KLF3) suppresses NF-kB−driven inflammation in mice. *J Biol Chem* 295: 680−691

Knights AJ, Yik JJ, Mat Jusoh H, Norton LJ, Funnell AP, Pearson RC, Bell-Anderson KS, Crossley M, Quinlan KG (2016) Kruppel-like Factor 3 (KLF3/BKLF) is required for widespread repression of the Inflammatory Modulator Galectin-3 (Lgals3). *J Biol Chem* 291: 16048−16058

Kohlgruber AC, Gal-Oz ST, LaMarche NM, Shimazaki M, Duquette D, Koay HF, Nguyen HN, Mina AI, Paras T, Tavakkoli A *et al* (2018) gammadelta T cells producing interleukin-17A regulate adipose regulatory T cell homeostasis and thermogenesis. *Nat Immunol* 19: 464−474

Koster J, Rahmann S (2012) Snakemake–a scalable bioinformatics workflow engine. *Bioinformatics* 28: 2520−2522

Lamkin DM, Ho HY, Ong TH, Kawanishi CK, Stoffers VL, Ahlawat N, Ma JCY, Arevalo JMG, Cole SW, Sloan EK (2016) beta-Adrenergic-stimulated macrophages: comprehensive localization in the M1–M2 spectrum. *Brain Behav Immun* 57: 338−346

Li B, Dewey CN (2011) RSEM: accurate transcript quantification from RNA-Seq data with or without a reference genome. *BMC Bioinformatics* 12: 323

Martin M (2011) Cutadapt removes adapter sequences from high-throughput sequencing reads. *EMBnet J* 17: 3

McInnes L, Healy J, Melville J (2018) UMAP: Uniform manifold approximation and projection for dimension reduction. *arXiv* https://arxiv.org/abs/1802. 03426v2 [PREPRINT]

Morrison SF (2016) Central neural control of thermoregulation and brown adipose tissue. *Auton Neurosci* 196: 14−24

Muthu K, Iyer S, He LK, Szilagyi A, Gamelli RL, Shankar R, Jones SB (2007) Murine hematopoietic stem cells and progenitors express adrenergic receptors. *J Neuroimmunol* 186: 27−36

Nguyen KD, Qiu Y, Cui X, Goh YP, Mwangi J, David T, Mukundan L, Brombacher F, Locksley RM, Chawla A (2011) Alternatively activated macrophages produce catecholamines to sustain adaptive thermogenesis. *Nature* 480: 104−108

Ohyama K, Nogusa Y, Shinoda K, Suzuki K, Bannai M, Kajimura S (2016) A synergistic antiobesity effect by a combination of capsinoids and cold temperature through promoting beige adipocyte biogenesis. *Diabetes* 65: 1410−1423

Olofsson PS, Steinberg BE, Sobbi R, Cox MA, Ahmed MN, Oswald M, Szekeres F, Hanes WM, Introini A, Liu SF *et al* (2016) Blood pressure regulation by CD4(+) lymphocytes expressing choline acetyltransferase. *Nat Biotechnol* 34: 1066−1071

Pirzgalska RM, Seixas E, Seidman JS, Link VM, Sánchez NM, Mahú I, Mendes R, Gres V, Kubasova N, Morris I *et al* (2017) Sympathetic neuron-associated macrophages contribute to obesity by importing and metabolizing norepinephrine. *Nat Med* 23: 1309−1318

Qiao X, Kim DI, Jun H, Ma Y, Knights AJ, Park MJ, Zhu K, Lipinski JH, Liao J, Li Y *et al* (2019) Protein arginine methyltransferase 1 interacts with PGC1alpha and modulates thermogenic fat activation. *Endocrinology* 160: 2773−2786

Rajbhandari P, Arneson D, Hart SK, Ahn IS, Diamante G, Santos LC, Zaghari N, Feng AC, Thomas BJ, Vergnes L *et al* (2019) Single cell analysis reveals immune cell-adipocyte crosstalk regulating the transcription of thermogenic adipocytes. *Elife* 8: e49501

Rajbhandari P, Thomas BJ, Feng A-C, Hong C, Wang J, Vergnes L, Sallam T, Wang BO, Sandhu J, Seldin MM *et al* (2018) IL-10 signaling remodels adipose chromatin architecture to limit thermogenesis and energy expenditure. *Cell* 172: 218−233.e17

Reardon C, Duncan GS, Brustle A, Brenner D, Tusche MW, Olofsson PS, Rosas-Ballina M, Tracey KJ, Mak TW (2013) Lymphocyte-derived ACh regulates local innate but not adaptive immunity. *Proc Natl Acad Sci U S A* 110: 1410−1415

Rosas-Ballina M, Olofsson PS, Ochani M, Valdes-Ferrer Si, Levine YA, Reardon C, Tusche MW, Pavlov VA, Andersson U, Chavan S *et al* (2011) Acetylcholine-synthesizing T cells relay neural signals in a vagus nerve circuit. *Science* 334: 98−101

Scanzano A, Cosentino M (2015) Adrenergic regulation of innate immunity: a review. *Front Pharmacol* 6: 171

Scheja L, Heeren J (2019) The endocrine function of adipose tissues in health and cardiometabolic disease. *Nat Rev Endocrinol* 15: 507−524

Shi J, Hua L, Harmer D, Li P, Ren G (2018) Cre driver mice targeting macrophages. *Methods Mol Biol* 1784: 263−275

Song P, Mabrouk OS, Hershey ND, Kennedy RT (2012) In vivo neurochemical monitoring using benzoyl chloride derivatization and liquid chromatography-mass spectrometry. *Anal Chem* 84: 412−419

Villarroya F, Cereijo R, Villarroya J, Gavalda-Navarro A, Giralt M (2018) Toward an understanding of how immune cells control brown and beige adipobiology. *Cell Metab* 27: 954−961

Xiong X, Kuang H, Ansari S, Liu T, Gong J, Wang S, Zhao X-Y, Ji Y, Li C, Guo L *et al* (2019) Landscape of intercellular crosstalk in healthy and NASH liver revealed by single-cell secretome gene analysis. *Mol Cell* 75: 644−660.e5

Yabut JM, Desjardins EM, Chan EJ, Day EA, Leroux JM, Wang BO, Crane ED, Wong W, Morrison KM, Crane JD *et al* (2020) Genetic deletion of mast cell serotonin synthesis prevents the development of obesity and insulin resistance. *Nat Commun* 11: 463

Yona S, Kim K-W, Wolf Y, Mildner A, Varol D, Breker M, Strauss-Ayali D, Viukov S, Guilliams M, Misharin A *et al* (2013) Fate mapping reveals origins and dynamics of monocytes and tissue macrophages under homeostasis. *Immunity* 38: 79−91

Zhang X, Wang X, Yin H, Zhang L, Feng A, Zhang Q-X, Lin Y, Bao B, Hernandez LL, Shi G-P *et al* (2019) Functional inactivation of mast cells enhances subcutaneous adipose tissue browning in mice. *Cell Rep* 28: 792−803.e4

Zhou Y, Zhou B, Pache L, Chang M, Khodabakhshi AH, Tanaseichuk O, Benner C, Chanda SK (2019) Metascape provides a biologist-oriented resource for the analysis of systems-level datasets. *Nat Commun* 10: 1523

Zhu L, Tang Y, Li X-Y, Keller ET, Yang J, Cho J-S, Feinberg TY, Weiss SJ (2020) Osteoclast-mediated bone resorption is controlled by a compensatory network of secreted and membrane-tethered metalloproteinases. *Sci Transl Med* 12: eaaw6143